

Structural optimization of magnetic flux concentrator based on particle swarm optimization algorithm

Yu-Xiao Wang(王雨潇), Shi-Yu Guan(管世钰), Yi Zhang(张燚), Qi-Yuan Jiang(江奇渊), Bing-Feng Sun(孙兵锋), and Zhong-Qi Tan(谭中奇)

Citation: Chin. Phys. B, 2026, 35 (**4**): 040701. DOI: 10.1088/1674-1056/ae0b38
http://cpb.iphy.ac.cn; http://iopscience.iop.org/cpb

What follows is a list of articles you may be interested in

Application of Gauss-Newton method in magnetic dipole model

Junchen Gao(高骏琛), Chaobo Liu(刘超波), Jinjing Zhang(张津菁), Yu Duan(段宇), Hao-Ran Yang(杨浩冉), and Daqiang Gao(高大强)

Chin. Phys. B, 2025, 34 (**10**): 100701. DOI: 10.1088/1674-1056/addcd1

Spin-based magnetic detection of optically trapped single cell in microfluidic channel

Jun Yin(殷俊), Sanyou Chen(陈三友), Yihao Yan(燕一皓), Mengqi Wang(王孟祺), Ya Wang(王亚), Yiheng Lin(林毅恒), Qi Zhang(张琪), and Fazhan Shi(石发展)

Chin. Phys. B, 2025, 34 (**7**): 070704. DOI: 10.1088/1674-1056/adde38

Realization of an optimized cylindrical uniform magnetic field coil via flexible printed circuit technology

A-Hui Zhao(赵阿慧), Yong-Le Zhang(张永乐), Yue-Yue Liang(梁跃跃), Yi Zhang(张艺), Jun-Jun Zha(查君君), Dao-Rong Rui(芮道荣), Xiao-Qiang Zhang(张肖强), and Kang Yang(杨康)

Chin. Phys. B, 2024, 33 (**12**): 120702. DOI: 10.1088/1674-1056/ad84c1

Performance optimization of a SERF atomic magnetometer based on flat-top light beam

Ziqi Yuan(袁子琪), Junjian Tang(唐钧剑), Shudong Lin(林树东), and Yueyang Zhai(翟跃阳)

Chin. Phys. B, 2024, 33 (**6**): 060703. DOI: 10.1088/1674-1056/ad401b

Response optimization of a three-axis sensitive SERF magnetometer for closed-loop operation

Yuanrui Zhou(周原锐), Yongze Sun(孙永泽), Xixi Wang(汪茜茜), Jianan Qin(秦佳男), Xue Zhang(张雪), and Yanzhang Wang(王言章)

Chin. Phys. B, 2024, 33 (**2**): 020701. DOI: 10.1088/1674-1056/ad0b00

Structural optimization of magnetic flux concentrator based on particle swarm optimization algorithm

Yu-Xiao Wang(王雨潇)[1,2], Shi-Yu Guan(管世钰)[1,2], Yi Zhang(张燚)[1,2], Qi-Yuan Jiang(江奇渊)[1,2], Bing-Feng Sun(孙兵锋)[1,2], and Zhong-Qi Tan(谭中奇)[1,2,†]

[1] *College of Advanced Interdisciplinary Studies, National University of Defense Technology, Changsha* 410073, *China*
[2] *Nanhu Laser Laboratory, National University of Defense Technology, Changsha* 410073, *China*

(Received 4 July 2025; revised manuscript received 5 September 2025; accepted manuscript online 25 September 2025)

This study introduces a structural optimization method for magnetic flux concentrators (MFCs) utilizing the particle swarm optimization (PSO) algorithm, addressing inefficiencies and challenges in achieving optimal structures with traditional methods. By integrating the PSO algorithm with COMSOL Multiphysics simulation software, a co-simulation framework is developed to optimize the parameters of a conical MFC. Compared with traditional methods, this approach enhances optimization results by twofold, achieving a magnetic field amplification factor of up to 200 within the defined parameter range. Additionally, an evaluation criterion for concentrator optimization is proposed, offering novel insights for designing concentrators across various scenarios.

Keywords: magnetic flux concentrator, magnetic sensing enhancement, particle swarm optimization

PACS: 07.55.Ge, 02.60.Pn, 75.50.–y, 87.55.de

DOI: 10.1088/1674-1056/ae0b38 **CSTR:** 32038.14.CPB.ae0b38

1. Introduction

Weak magnetic detection technology is a core precision measurement technique with widespread applications in scientific research and engineering. Its high sensitivity and nanometer-scale resolution make it indispensable for many fields including biomedical imaging,[1,2] geological exploration,[3,4] and quantum sensing.[5,6] For example, in fundamental physics, it resolves hyperfine magnetic interactions in quantum systems.[7] In industry, it enables defect detection in semiconductor manufacturing[8,9] and nondestructive inspection of electrical equipment.[10,11] Mainstream magnetic detection technologies encompass superconducting quantum interference devices (SQUIDs), giant magnetoresistance (GMR) sensors, nitrogenvacancy (NV) color center magnetometers, optical pumping magnetometers, and fluxgate magnetometers. To enhance detection sensitivity, researchers have proposed optimization strategies for these methods, such as increasing NV center concentrations,[12] optimizing SQUID gradiometer and pickup coil structures to reduce noise,[13] and leveraging light-induced narrowing to suppress magnetic resonance linewidth broadening in optical pumping magnetometers.[14] In addition, the introduction of a magnetic flux concentrator (MFC) offers a novel approach to enhance weak magnetic field detection. Its efficacy in boosting sensitivity has been demonstrated in Hall and magnetoresistive sensors.[15,16] This method does not require altering the material properties or complex microfabrication processes of devices, thereby ensuring broad applicability and compatibility. The MFC can be readily adapted to diverse sensor systems, such as Hall, magnetoresistive, and GMR sensors, with relatively low system complexity and technical barriers. Furthermore, the structure and size of the MFC can be easily adjusted to meet specific application requirements, which is advantageous in terms of cost and engineering implementation.

Flux concentrators enhance magnetic fields via magnetic flux convergence, demonstrating significant promise in integrated magnetometers. For instance, adopting a T-shaped flux concentrator in a magnetometer based on NV centers has been shown to improve sensitivity from 1.5 $\mathrm{nT}/\sqrt{\mathrm{Hz}}$ to 0.13 $\mathrm{nT}/\sqrt{\mathrm{Hz}}$.[17] Similarly, combining a flux concentrator with a SQUID in magneto-enterogram (MENG) systems can also enhance detection sensitivity, achieving a 9.86-fold increase in the magnetic field within a 0.2–1.0 Hz signal range with a variance of only 3.42%, thus more effectively assisting the diagnosis of acute mesenteric ischemia.[18] Furthermore, integrating a Hall sensor within a specially designed flux concentrator can increase the effective sensitivity by at least three orders of magnitude.[19] However, current designs of MFCs face several technical challenges, with two most notable being the limited amplification and lack of systematic optimization approaches. Currently, almost all MFCs used in various magnetometers adopt classic shapes, including conical, T-shaped, cylindrical, etc.[20] Although classical shapes have theoretically good flux-concentration effects, the extensive parameter combinations and enormous simulation requirements pose challenges for traditional optimization methods which attempt

[†]Corresponding author. E-mail: zhqitan@sina.com

© 2026 Chinese Physical Society and IOP Publishing Ltd. All rights, including for text and data mining, AI training, and similar technologies, are reserved.

to explore as many combinations as possible to identify the optimal parameters. In contrast, intelligent algorithms, with the capability for efficient search and rapid computation, are well-suited to address these issues, but most existing optimization studies focus solely on magnetic amplification without considering practical constraints such as volume limitations for integrated applications.

In current scientific research, intelligent algorithms have emerged as the driving force for transcending the limitations of traditional methodologies. By emulating natural laws or biological intelligence, these algorithms offer a novel paradigm for modeling, optimization, and the prediction of scientific problems. The suitability of different intelligent algorithms is contingent on their unique characteristics and the specific application scenarios. For instance, deep learning algorithms have been employed in gene sequence analysis,[21] climate model prediction,[22] and autonomous driving path planning through reinforcement learning mechanisms.[23] Similarly, genetic algorithms have been utilized to optimize multispectral camouflage adjustable multilayer film metamaterials with thermal management functions, thereby enhancing laser stealth capabilities by simulating the biological evolution process.[24] Additionally, the simulated annealing algorithm has been applied in drug design research to identify molecules with high binding affinity to specific target protein pockets.[25]

Among various intelligent algorithms, the particle swarm optimization (PSO) algorithm is widely applied to multi-objective optimization problems (MOPs) due to its high efficiency and implementation simplicity, such as in fields like production scheduling, power system planning, and image processing.[26] Compared to the traditional control variates method,[20] PSO facilitates multi-parameter collaborative optimization via a global search, enhancing the magnetic field amplification factor while reducing volume redundancy, offering a novel approach for optimizing the structure of MFCs. In contrast to other intelligent algorithms, PSO presents some distinct advantages. Group parallel searching of PSO enables rapid parameter space traversal, unlike the genetic algorithm's lengthy iterative convergence due to chromosome crossover.[27] In addition, in scenarios requiring dynamic topology adjustments of MFCs, PSO's inertia weight adjustment mechanism adeptly balances global exploration with local exploitation, unlike the simulated annealing algorithm, which may accept inferior solutions during high-temperature transitions.[28] Lastly, PSO's dual memory mechanism, incorporating individual and group optima, effectively overcomes the local optimum trap of traditional gradient descent methods.[29]

This study presents the basic principles of MFCs and their applications, employing PSO coupled with the multi-physics simulation tool COMSOL to comprehensively analyze the global optimization of the concentrator's geometric parameters. The optimized concentrator design is experimentally validated, demonstrating the efficacy of the proposed methodology. Furthermore, a performance evaluation index for MFCs is introduced, highlighting the need for future research to investigate the influence of factors such as manufacturing complexity and temperature stability, thereby enhancing the practical and theoretical value of this work.

2. Principles

2.1. MFC

MFCs are essential structures that enhance the sensitivity of magnetic sensors, whose primary function is to converge magnetic field lines and amplify the magnetic field through tailored geometric shapes and material properties. These devices are typically fabricated using soft magnetic alloys with high permeability and low coercivity. The manufacturing process often involves mechanical cutting followed by annealing to improve the hysteresis characteristics of the soft magnetic material. Permalloy, composed of iron, nickel, and cobalt, is the most commonly used material due to its relative magnetic permeability reaching the order of 10^4.[30,31] This property makes permalloy particularly suitable for applications requiring magnetic shielding, such as the measurement of weak magnetic fields. Alternatively, Mn–Zn ferrite, with a slightly lower permeability of several thousand,[32] offers high resistivity, reducing eddy current losses and minimizing magnetic noise from thermal fluctuations.

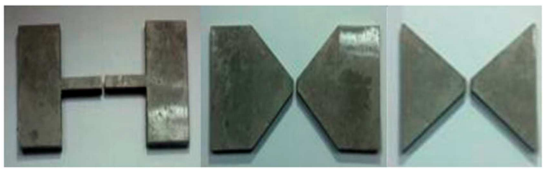


Fig. 1. MFC of T-shape, pentagon-shape and cone-shape.[20]

When a ferromagnetic material is subjected to an external magnetic field H_0', an opposing demagnetizing field H_D' is generated within it. Consequently, the total magnetic field inside the material becomes

$$H' = H_0' + H_D'. \tag{1}$$

For a homogeneous and isotropic ferromagnetic material, the demagnetizing field generated inside the material equals[33]

$$H_D' = -N_d M', \tag{2}$$

where N_d is the demagnetization factor related to the geometric shape and size of the material. $M' = \chi H'$ is the magnetization. χ is the magnetic susceptibility with $\chi = \mu_R - 1$. Considering only the intensity in the direction of the external magnetic field H_0', the ratio of the actual magnetic induction intensity B in the presence of this ferromagnetic material to the

magnetic induction intensity B_0 of the external magnetic field in the absence of this ferromagnetic material is defined as[34]

$$G = \frac{B}{B_0} = \frac{\mu_0 \mu_R |H'|}{\mu_0 |H_0'|} = \frac{\mu_R}{1 + N_d (\mu_R - 1)}, \tag{3}$$

where μ_0 is the vacuum permeability and μ_R is the relative permeability of the material. When the relative permeability of the material is high enough, the above equation simplifies to

$$G \approx \frac{1}{N_d}. \tag{4}$$

For spherical materials, N_d usually equals $1/3$,[35] but the geometry can be designed to decrease the value of N_d,[34] thereby enhancing the magnetic field. In most ferromagnetic materials with more intricate geometries, analytical solutions for N_d are unavailable, necessitating finite element software for numerical simulations to solve G directly. This approach enables the amplification of the external magnetic field through the design of specialized ferromagnetic materials.

2.2. PSO

The PSO algorithm is a metaheuristic inspired by the cooperative foraging behavior of social animals, such as flocks of birds or schools of fish. By observing these natural systems, researchers have found that the sharing of information within a group confers evolutionary advantages, which can be leveraged to achieve global optimization in scientific problems. In the PSO algorithm, each particle represents a potential solution, and the algorithm simulates the particle's velocity and position updates within the solution space. The particle's motion is driven by both its individual historical optimal solution (governed by cognitive coefficients) and the global optimal solution of the population (governed by social coefficients). In each iteration, the particle updates its velocity and position according to the following rules:

$$v_i^{t+1} = \omega \cdot v_i^t + c_1 \cdot r_1 \cdot \left(p_{\text{best},i} - x_i^t\right) + c_2 \cdot r_2 \cdot \left(g_{\text{best}} - x_i^t\right), \tag{5}$$

$$x_i^{t+1} = x_i^t + v_i^{t+1}, \tag{6}$$

where v_i^t and x_i^t are the velocity and position of the particle i at the t^{th} iteration, respectively. ω represents the inertia weight. c_1 and c_2 are the cognitive and social coefficients, respectively. r_1 and r_2 are the random numbers inside $[0, 1]$. By establishing the connection between each particle and the individual's historical optimal position $p_{\text{best},i}$ and the group's global optimal position g_{best}, the particle swarm gradually moves to the high-quality solution area.

3. Modeling and optimization

This work takes the conical flux concentrator as an example to establish and validate the PSO-COMSOL optimization framework. The PSO-COMSOL framework developed here provides the essential foundation for future extensions to other geometries. The optimization of the conical flux concentrator employs a PSO algorithm, which can be divided into three phases: modeling and simulation, algorithm optimization, and verification feedback. This process forms a closed loop, with the optimization results evaluated through two validation steps: simulation validation and experimental validation, as illustrated in Fig. 2.

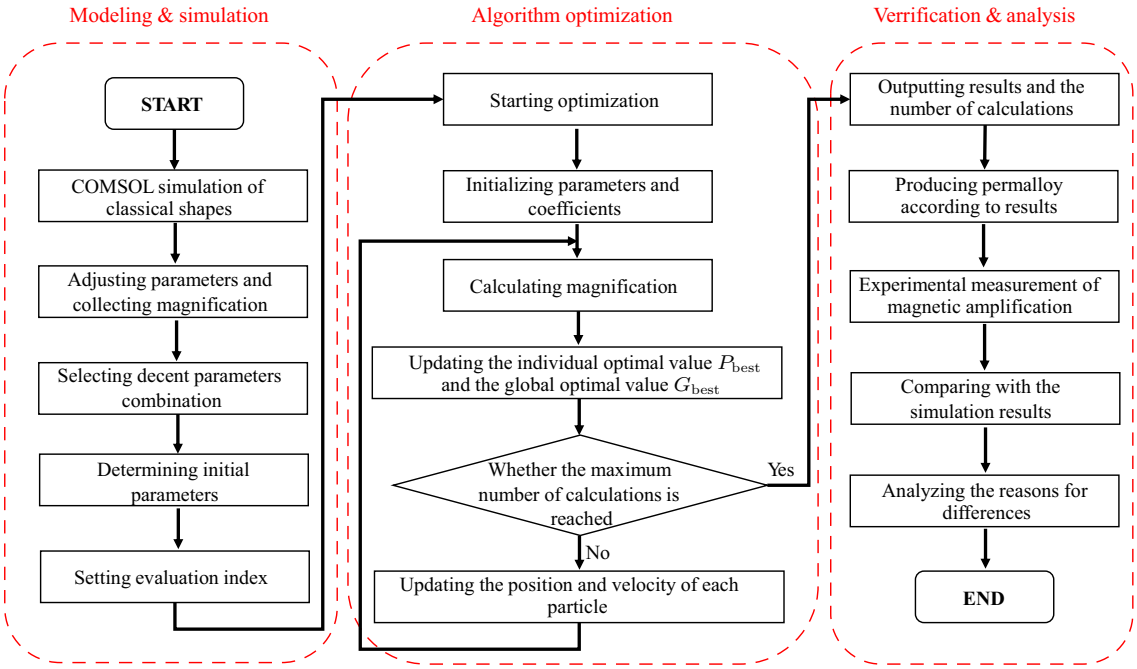


Fig. 2. PSO process.

3.1. COMSOL modeling and verification of magnetic field amplification

To optimize the design of the MFC, a 3D axisymmetric finite element model was developed in COMSOL Multiphysics to verify the magnetic amplification effect. The model mainly consists of two symmetrically arranged conical soft magnetic alloy (permalloy) components, fixed on both sides of an air gap, with a uniform background magnetic field applied along the Z-axis in the external air domain. To minimize computational load, the conical cross-section was initially drafted in the plane, then symmetry and rotation were applied to achieve the complete geometry, as illustrated in Fig. 3. The geometric specifications include a 20 mm radius at the cone base, a 1 mm radius at the top, a height of 20 mm, and a 1 mm air gap width. Permalloy was selected to simulate the magnetic flux convergence properties of the soft magnetic material.

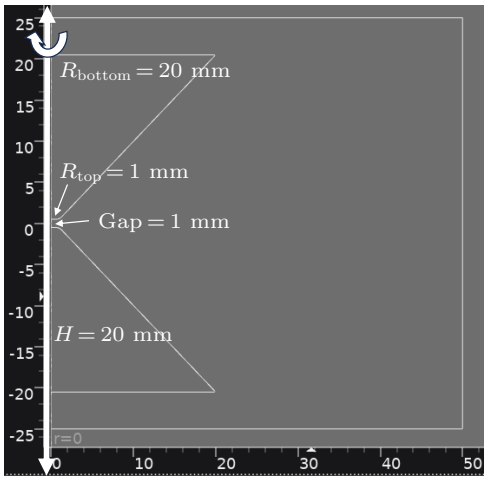


Fig. 3. Conical section model.

The magnetic field (mf) module is employed to better describe and construct the physical field. Firstly, modeling the environment around the concentrator, where the air domain is defined as free space, is used to specify the physical conditions in the vicinity of the device. Secondly, the axisymmetric condition is applied to the conical geometric cross-section. This ensures that the axis of symmetry adheres to either the zero Neumann condition or the no-flux condition, aligning the geometric configuration with real-world physical scenarios. Additionally, to designate the study area within the air domain, the magnetic insulation condition must be set for the air domain boundary. This entails setting the tangential component of the magnetic vector potential at the boundary to zero as follows:

$$n \times A = 0. \tag{7}$$

Equation (7) indicates that the tangential component of the vector potential at the material surface is zero. This implies that the magnetic field circulation remains constant at this boundary, thereby preventing magnetic flux from crossing it. This condition serves to simplify the model and guarantee the attainment of the intended magnetic field configuration in the simulation. Particularly in intricate electromagnetic field analyses involving magnetic materials, it plays a crucial role in regulating the magnetic field distribution, refining design optimization, and enhancing simulation accuracy.

Ampere's law in solids is applied to the two conical flux concentrators in order to accurately model the magnetic field in and around the conical concentrators. This model integrates the intrinsic properties of magnetic materials and considers the effects of metal geometry, material properties such as conductivity and permeability, and other factors, yielding a realistic depiction of the magnetic field distribution. The relations are as follows:

$$\nabla \times H = J, \tag{8}$$

$$B = \nabla \times (A_{\text{b}} + A_{\text{r}}), \tag{9}$$

$$J = \sigma E, \tag{10}$$

$$B = \mu_0 \mu_{\text{r}} H, \tag{11}$$

$$D = \varepsilon_0 \varepsilon_{\text{r}} E. \tag{12}$$

Equation (8) indicates that the curl of magnetic field H equals the current density J, which shows how current generates a magnetic field and is the basis for modeling magnetic interactions. Equation (9) defines the relationship between the magnetic field B and the vector potential (A_{b} and A_{r}). Vector potentials are mathematical representations that simplify electromagnetic theory calculations, and their sum indicates the contributions from different sources or regions. Equation (10) shows that current density J is proportional to the electric field E, indicating the material's response to the applied electric field, where σ is the conductivity of the material, and thus affects the overall magnetic field distribution. Equations (11) and (12) are constitutive relationships, showing that the magnetic induction intensity is affected by the nature of the material and that the electrical properties of the material have a direct effect on the electric displacement vector. μ_0, μ_{r}, ε_0, and ε_{r} represent the magnetic permeability of free space, the relative magnetic permeability, the dielectric constant of free space, and the relative dielectric constant, respectively.

The mesh division employs an adaptive dissection strategy, strengthening the mesh at the MFC tip region while loosening it in the air domain to optimize accuracy and computational speed for magnetic field gradient calculations. Figure 4 illustrates the simulation results, demonstrating the convergence of magnetic lines at the MFC tip and achieving over ninefold magnetic field amplification. This confirms the feasibility of the simulated flux concentrator in amplifying the magnetic field.

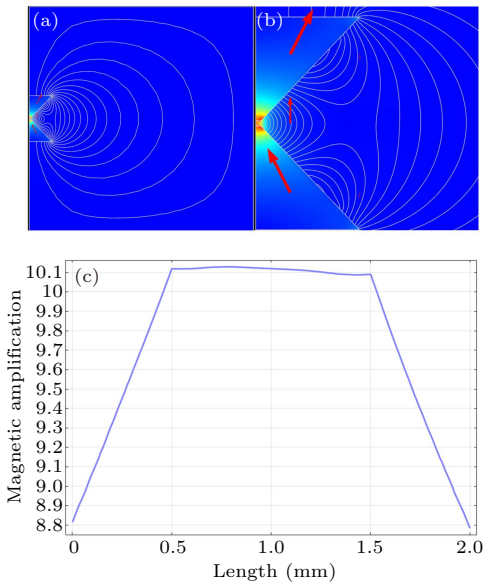


Fig. 4. Simulation results of conical flux concentrator: (a)–(b) the concentration of magnetic lines with the MFC, and (c) magnetic amplifications at different lengths in the gap.

3.2. PSO based on COMSOL simulation

To efficiently optimize the structure of the flux concentrator, this study employs a co-simulation framework, integrating PSO with multi-physics field modeling. The process focuses on parametric modeling, algorithm optimization, and data interaction, optimizing the flux concentrator structure through iterative algorithms. The specific implementation steps are as follows. Set key dimensional parameters including top radius R_{top}, bottom radius R_{bottom}, height H, and gap d. Adjust the values of these parameters and simulate the magnetic induction intensity at the center of the two concentrators in the COMSOL model, and the magnetic amplification factor is calculated. The simulation results, as shown in Fig. 5, demonstrate a significant enhancement of the magnetic induction intensity when $R_{\text{top}} = 2$ mm, $R_{\text{bottom}} = 20$ mm, $H = 20$ mm and $d = 5$ mm, achieving a magnetic amplification of 18 times.

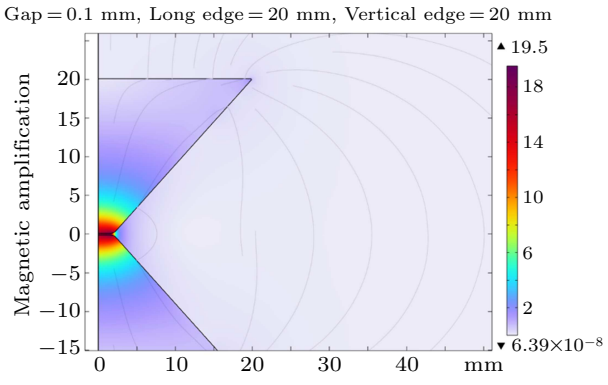


Fig. 5. Simulation results of the magnetic field intensity $|B|$ of the conic concentrator.

The concentrator above notably enhances the magnetic field, thereby improving the magnetometer's sensitivity. However, it falls short of expectations, indicating the potential for further optimization. Table 1 presents some finite element simulation results for various parameter combinations.

Table 1. Simulation results of some selected parameter combinations.

	Height	Bottom radius	Top radius	Gap	Amplification
Set 1	10 mm	10 mm	1 mm	1 mm	13.69
Set 2	15 mm	20 mm	2 mm	1.5 mm	13.42
Set 3	30 mm	20 mm	3 mm	1.5 mm	22.83
Set 4	30 mm	20 mm	2 mm	3 mm	12.62
Set 5	40 mm	30 mm	3 mm	3 mm	17.91
Set 6	40 mm	30 mm	3 mm	4 mm	13.44
Set 7	40 mm	30 mm	3 mm	1 mm	41.40
Set 8	40 mm	40 mm	3 mm	1 mm	45.68
Set 9	50 mm	40 mm	3 mm	1 mm	58.18
Set 10	50 mm	40 mm	2 mm	1 mm	63.73
Set 11	50 mm	50 mm	2 mm	1 mm	64.42
Set 12	50 mm	60 mm	2 mm	1 mm	59.08

The data presented in the table suggests an empirical relationship. As the cone's height increases, the base radius increases, the top radius decreases, and the gap narrows, leading to greater magnetic amplification. Based on this observed trend, an initial set of parameter values was selected to serve as a reasonable starting point for the optimization process, guiding the algorithm towards a more promising optimization direction and reducing computational effort: $R_{\text{top}} = 2$ mm, $R_{\text{bottom}} = 50$ mm, $H = 50$ mm, and $d = 1$ mm. This set of parameters is then used as the initial shape for optimization, and the particle swarm algorithm is used to optimize the shape within the parameter ranges: $R_{\text{top}} \in [1,8]$ mm, $R_{\text{bottom}} \in [10,50]$ mm, $H \in [10,60]$ mm, and $d \in [1,5]$ mm.

The above approach confirms the viability of employing the flux concentrator for magnetic field amplification and establishes the initial optimization value. Subsequently, the algorithm is used to interface with COMSOL Livelink, facilitating the control of COMSOL to define parameters, construct geometry, select materials, set up physical fields, configure solvers, and read results, thereby completing the model development. Key parameters in the algorithm are then determined, including the cognitive coefficient c_1, social coefficient c_2, and inertia weight ω. The cognitive coefficient specifically adjusts the particle's reliance on its historical best position. Among them, the cognitive coefficient c_1 modulates a particle's reliance on its historical optimal position. A high cognitive coefficient, for example $c_1 > 3$, enhances local search capabilities but may restrict the search range and lead to local optima. Conversely, a very low cognitive coefficient diminishes the impact of individual experience, reducing convergence efficiency. The social coefficient c_2 governs particle convergence towards the group's optimal solution. A high social coefficient, for example $c_2 > 3$, accelerates population convergence but risks premature convergence, while a low social coefficient limits information sharing, impairing global exploration. Inertia weight ω influences the continuity

of particles' motion direction. A high inertia weight (e.g., 0.9) broadens the exploration range, whereas a low inertia weight (e.g., 0.3) improves local exploitation precision. To enhance initial exploration and accelerate late-stage convergence, the following parameter settings are set: $\omega_{\max} = 0.9$, $\omega_{\min} = 0.4$, $c_{1_initial} = 2.0$, $c_{2_initial} = 1.5$, $c_{1_final} = 0.5$, $c_{2_final} = 3.0$. As the algorithm progresses, the cognitive coefficient decreases nonlinearly, while the social coefficient increases nonlinearly, as follows:

$$\omega = \omega_{\max} - (\omega_{\max} - \omega_{\min}) \times p, \tag{13}$$

$$c_1 = c_{1_initial} - (c_{1_initial} - c_{1_final}) \times p^2, \tag{14}$$

$$c_2 = c_{2_initial} + (c_{2_final} - c_{2_initial}) \times p^2, \tag{15}$$

$$p = i/n_{\text{iterations}}, \tag{16}$$

where p denotes the iteration process, i is the number of iterations, and $n_{\text{iterations}}$ is the total number of iterations.

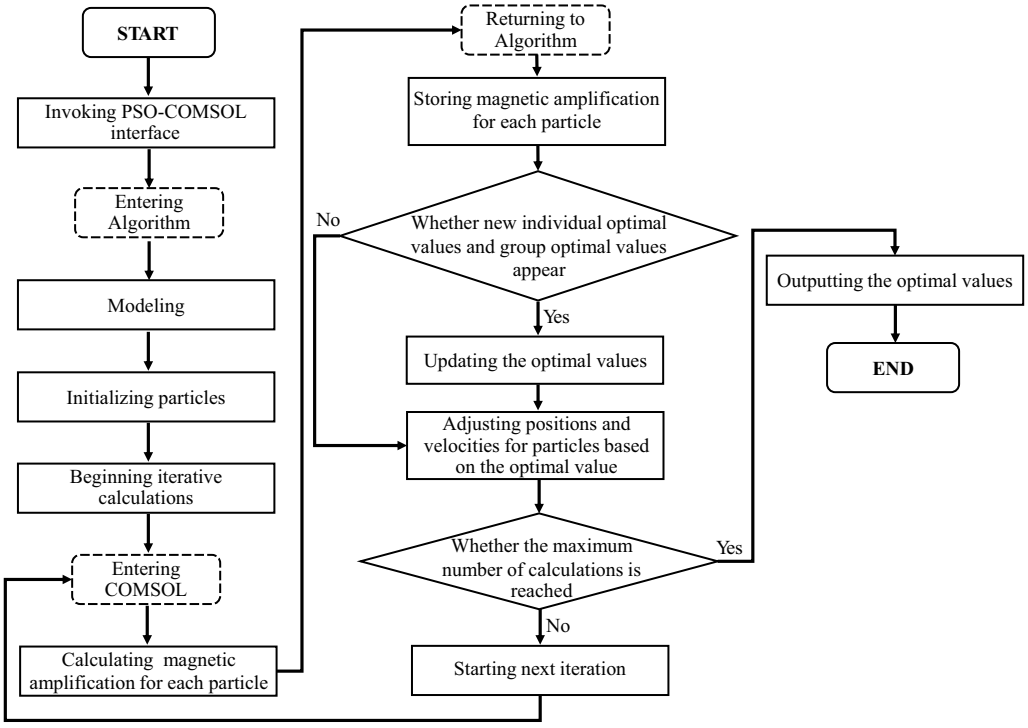


Fig. 6. Co-simulation of COMSOL with PSO algorithm.

Table 2. Simulation results of PSO algorithm.

Calculations	Height (mm)	Bottom radius (mm)	Top radius (mm)	Gap (mm)	Amplification	Volume r (mm^3)
24	60.0000	50.0000	1.0000	1.0000	82.18	160202.80
50	59.9687	50.0000	1.0031	1.0000	83.22	160129.35
100	53.8333	21.8756	3.2749	1.1361	100.55	31604.61
150	60.0000	28.7559	1.6621	1.0000	117.34	55104.50
200	60.0000	50.0000	1.4129	1.0000	117.62	161561.87
300	60.0000	33.2527	1.5308	1.0000	123.25	72784.49
450	60.0000	30.4374	1.0000	1.0000	124.34	60154.41
800	58.4250	50.0000	5.2962	1.0000	171.52	170787.56
1500	60.0000	44.4394	3.5861	1.0000	164.60	134836.91
2400	58.7443	48.4274	4.4530	1.0022	179.57	158675.50
3200	60.0000	49.2902	4.4197	1.0015	187.46	167481.66
4600	60.0000	50.0000	7.3550	1.0000	186.29	183491.93
5600	60.0000	50.0000	7.2545	1.0000	211.83	183084.15

The below figure shows the basic flow of PSO combined with COMSOL for optimization. The process begins with a predefined initial value, introduces random perturbations, and assigns values to all particles in the population. Subsequently, the model calculates the magnetic amplification for each of these particles. This information is fed back into the algorithm to initiate the next iteration. In each new iteration, particles are adjusted based on both individual and collective historical optima, as defined by Eqs. (5) and (6). New parameter combinations are then generated, reassigned to the particles, and

re-evaluated in the COMSOL simulation to obtain the magnetic amplification, continuing this iterative process. The advantage of the mentioned method lies in the population's ability to solve the optimization problem by emulating the foraging behavior of bird flocks. This approach leverages information sharing and mutual learning among individuals, allowing them to adjust positions based on personal and collective experiences. Conversely, the traditional control variates method relies on fixed parameter intervals, employing control variables for traversal calculations. Here, the particle swarm algorithm optimizes the data sets presented in Table 2.

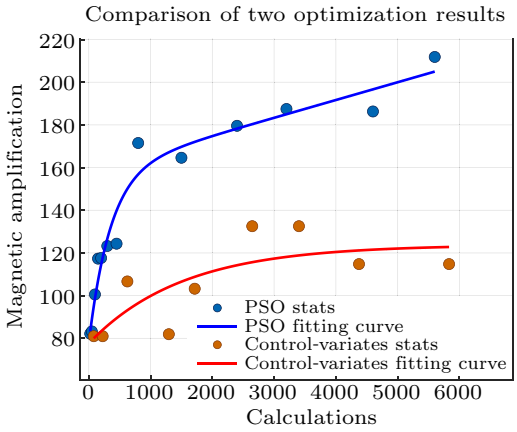


Fig. 7. Comparison of two optimization results.

The optimization results depicted in Fig. 7 demonstrate the superior performance of the PSO method compared to the traditional approach. The solid points represent the magnetic amplification achieved after optimization with several calculations, while the solid line fits the trend of the optimization results. The blue solid points correspond to the findings summarized in Table 2. As illustrated in the figure, the PSO approach can achieve a magnetic field magnification of approximately 110 times with only around 150 calculations. In contrast, the traditional control variates method, which relies on manually selecting parameter traversal intervals, lacks the ability to reliably identify an effective optimization direction. This results in the magnetic magnification not increasing steadily as the number of calculations increases, while the computational complexity continues to rise. Consequently, the traditional method requires thousands of calculations to reliably reach a magnetic magnification over 110 times. Notably, the PSO algorithm can obtain a magnetic magnification approximately twice that of the traditional way, utilizing the same computational resources. These results clearly indicate that the PSO approach is a more effective optimization strategy. Furthermore, previous research[36] has reported a magnetic magnification of 18.21 times for a T-shaped concentrator at a spacing of 0.5 mm. In contrast, the parameter range set in the current optimization is relatively narrow, with a minimum spacing of 1 mm, yet the optimal result can still reach around 210. This suggests that by expanding the parameter range, the size of the optimized concentrator may increase; this allows for the concentration of even stronger magnetic fields in the central area, potentially leading to further optimization and the achievement of even larger magnetic amplifications.

3.3. Expanded application

As a competitive room temperature magnetometer platform with excellent spatial resolution, dynamic range and sensitivity, the NV color center magnetometer requires neither cryogenics nor heating in operation, and the sensor can be scaled down to the size of the diamond itself.[36,37] In the meantime, the flux concentrator plays a crucial role in enhancing the magnetic field within the NV color center magnetometer probe. The size and magnetic field amplification capability of the flux concentrator are key factors to consider, as an overly large flux concentrator can lead to an increase in the overall size of the magnetometer probe, consequently reducing its spatial resolution. To address this issue, a comprehensive evaluation index for the flux concentrator is essential. Optimizing the structure of the concentrator can be achieved using a PSO algorithm to meet the practical application requirements effectively. Thus, our study establishes an evaluation criterion, for example,

$$p = c_1 \times \frac{1}{V} + c_1 \times M + \cdots, \tag{17}$$

where P is the evaluation index, V is the volume, M is the magnetic field amplification, and c_1, c_2 are weighted factors (here set to 0.7 and 0.3). By adjusting the weighted factors, the relative importance of different influencing factors like volume and amplification can be fine-tuned, enabling the assessment of the efficacy of the designed flux concentrator based on a comparative analysis of these indices.

Unlike conventional approaches that optimize purely for maximum magnetic amplification, the above multi-objective evaluation framework considers both magnetic enhancement performance and spatial constraints. While the mathematical expression appears simple, this represents the first systematic approach to integrate volume limitations with amplification optimization, providing a new paradigm for practical MFC design in space-constrained applications such as integrated diamond NV magnetometers.

The optimization process, depicted in Fig. 8, takes into account the impact of volume by constraining the four parameters within a specific range: $R_{\text{top}} \in [1,8]$ mm, $R_{\text{bottom}} \in [30,60]$ mm, $H \in [20,100]$ mm, and $d \in [1,5]$ mm. Compared in Table 2, the optimal parameters of the flux concentrator, considering only the magnetic amplification, are not the same as those after incorporating the effect of volume. Furthermore, there is even a significant difference, which indicates that different flux concentrators should be designed for different application scenarios. For maximal magnetic field amplification,

the concentrator characterized by higher magnetic amplification in Table 2 is preferable. Conversely, if the concentrator is intended for use in a compact magnetic field probe, the design illustrated in Fig. 8 proves more effective.

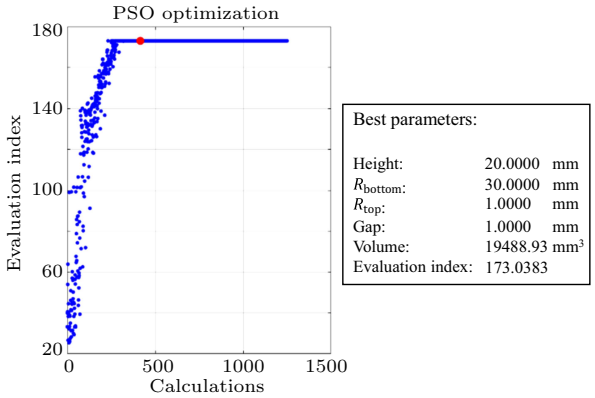


Fig. 8. Optimization after considering volume.

4. Experimental verification

To verify the above theoretical part, a large three-axis Helmholtz coil (FE-3FM600, Hunan Yongyi Technology Co., Ltd.), which could provide a magnetic field ranging from ± 1.0 mT with uniformity better than 0.3%, was used to generate a magnetic field uniform region with a side length of 600 mm. An Afluxgate magnetometer (CH-330F, CH-Hall Magnetic Technology Co., Ltd.), which enabled magnetic field measurement with a resolution of 0.1 nT and a measurement accuracy of 0.5% of reading ± 10 nT, was used for magnetic field detection. Given that the fluxgate probe is a 20 mm cube, and the magnetic field amplification by the concentrator diminishes with increasing gap width,[20] the minimum air gap in the experiment was set to 21 mm to ensure that the probe is completely located at the center of the air gap of the MFC and to avoid the boundary effect between the probe edge and the inner wall of the concentrator from interfering with the test results. This ensured the spacing was minimized while remaining slightly larger than the fluxgate probe. Three sets of optimized parameters were obtained using the same method as in the modeling and optimization part. Permalloy 1J85 (initial permeability $\mu_0 \approx 60000$) was used as the material to fabricate MFCs with the above three structures for experimental verification. The support structure used in the experiment was made of aluminum alloy, so it would not affect the magnetic field distribution generated by the Helmholtz coil. The experimental setup is shown in Fig. 9.



Fig. 9. (a) Helmholtz coil FE-3FM600, and (b) FE-2100FG magnetic field control software and FE-500 — a high-precision programmable constant current DC power supply.

The experiment commenced with a zero-adjustment controlled by the host computer, followed by a systematic calibration and measurement protocol. First, without the flux concentrator in position, uniform magnetic fields of 0, 0.25, 0.4, and 0.5 Gauss were sequentially applied in the Z-direction using the Helmholtz coil system. The CH-330F fluxgate probe was positioned at the center of the coil to measure the magnetic field response along the Z-axis. For each field strength, the baseline response was calculated as the difference between field-on and field-off readings to establish reference values and eliminate spatial geomagnetic interference effects, as depicted in Fig. 10.

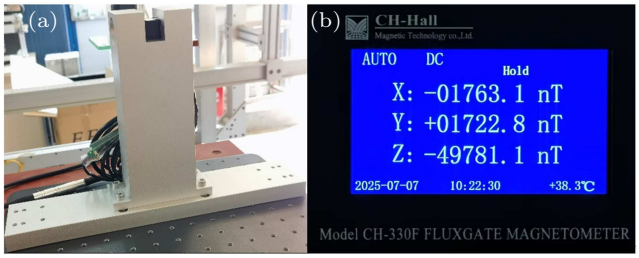


Fig. 10. Measuring the initial external magnetic field: (a) CH-330F fluxgate magnetometer and aluminum alloy support devices, and (b) magnetometer readings under a 0.5 Gauss magnetic field.

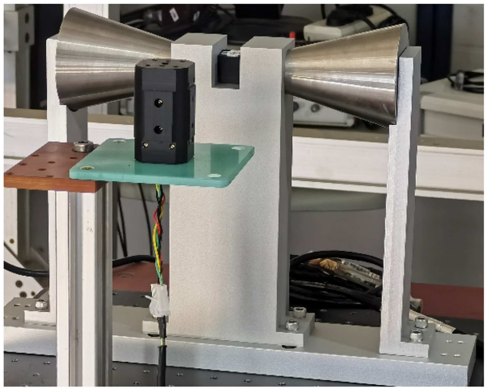


Fig. 11. MFC magnetic field enhancement measurement: positioning measurement device for permalloy conical concentrator ($d = 21$ mm gap) in magnetic field.

Subsequently, the flux concentrator was positioned at the measurement location, as shown in Fig. 11, and the same magnetic field sequence (0, 0.25, 0.4, 0.5 Gauss) was applied. The enhanced magnetic field responses were measured at the same probe location, with readings recorded and field variations calculated.

The actual magnetic amplification was determined as the ratio of the magnetic field variation with the concentrator to

that without the concentrator at each field strength, as shown in Table 3. This systematic approach ensures accurate quantification of the enhancement performance while eliminating the effects of concentrator remanence and sensor bias.

Table 3. Simulation and experimental results of three groups at the gap of 21 mm.

	Height	Bottom radius	Top radius	Simulation amplification	Experimental amplification	Deviation
Set 1	110 mm	38 mm	8 mm	6.3	6.2	1.6%
Set 2	131 mm	39 mm	7 mm	7.1	6.8	4.4%
Set 3	140 mm	47 mm	7 mm	7.6	7.3	4.1%

The experimental results demonstrate an amplification factor of approximately 7 under relatively large spacing conditions, with an negligible discrepancy between the actual and simulated outcomes. This verifies the feasibility of the structural optimization approach and reliably predicts the magnetic field amplification law of the MFC, confirming its validity for theoretical calculations in small air gap scenarios. The observed differences may be attributed to several factors, as follows. (1) Variations between the actual material properties and those used in the simulation. Specifically, the magnetic permeability of the permalloy is highly sensitive to its composition, heat treatment, and residual stress, often resulting in lower values than those assumed in the simulation. (2) Potential air gaps, loose assembly, or dimensional deviations during the fabrication process, which can increase magnetic resistance and reduce the efficiency of magnetic flux concentration. (3) Measurement uncertainties arising from the small applied magnetic field, such as sensor calibration errors, external magnetic field interference (fluctuating geomagnetism, nearby electrical equipment), and temperature changes. Solely relying on the host computer's closed-loop control for zero adjustment may be insufficient to eliminate these interferences completely. (4) Factors such as temperature, mechanical stress, and magnetostriction, which can alter magnetic properties, are often inadequately considered in simulations.

The influence of manufacturing tolerances on the performance of concentrators, which was a topic of constant interest, was investigated through a sensitivity analysis. Considering the limitations of actual machining accuracy, simulation studies were conducted on the key geometric parameters of three concentrator sets (Set 1, Set 2, Set 3) within a ± 0.5 mm tolerance range. The effect of the variation of each parameter within the tolerance range on the magnetic amplification was calculated. For the concentrators in Set 1, the deviations in the magnetic amplification caused by the variations in height, bottom radius, and top radius were 0.29%, 0.28%, and 0.52%, respectively. In Set 2, the corresponding deviations were 0.36%, 0.42%, and 0.80%. For Set 3, the deviations were 0.20%, 0.12%, and 0.71%. (Detailed results are provided in the Appendix.) The analysis reveals that all three designed concentrator groups demonstrate good manufacturing robustness. Under the practically attainable machining tolerance of ± 0.5 mm, the performance variations of all concentrators remain within the 5% error margin acceptable for general engineering applications. Notably, the top radius significantly affects the magnetic amplification, aligning with the mechanism of magnetic flux density concentration at the concentrator's apex. Therefore, in manufacturing, priority should be given to ensuring the precision of the top radius.

5. Conclusions

This paper introduces a novel multi-objective structural optimization approach for a MFC utilizing the PSO algorithm. Through a comprehensive integration of PSO with a multi-physics field simulation tool, an effective global optimization of the MFC's size parameters is realized. The proposed PSO-COMSOL co-simulation framework demonstrates significant advantages over traditional optimization methods, achieving approximately twice the magnetic amplification efficiency. Moreover, the introduced multi-objective evaluation criterion provides a systematic approach for balancing performance and practical constraints in MFC design. The optimized parameter structure is validated experimentally, demonstrating a strong agreement between the measured amplification and simulation results, which fully proves the effectiveness and practical value of the method.

In summary, this study presents efficient and intelligent optimization strategies for the design of MFCs, which hold significant theoretical and practical implications for enhancing the performance of weak magnetic sensing systems. Factors such as processing parameters and temperature stability can be further integrated to promote the optimal design of MFCs across diverse application scenarios.

Appendix A

The variations in magnetic amplification factors of the three groups concentrators under the tolerance of ± 0.5 mm are shown in the following table.

Tolerance analysis of the height of Set 1			
	H_2	$H_2 - 0.5$ mm	$H_2 + 0.5$ mm
H_1	**6.35**	6.32	6.33
$H_1 - 0.5$ mm	6.33	6.31	6.32
$H_1 + 0.5$ mm	6.33	6.35	6.36

Tolerance analysis of the bottom radius of Set 1			
	R_{base2}	$R_{base2}-0.5$ mm	$R_{base2}+0.5$ mm
R_{base1}	**6.35**	6.32	6.35
$R_{base1}-0.5$ mm	6.32	6.31	6.34
$R_{base1}+0.5$ mm	6.33	6.34	6.37

Tolerance analysis of the top radius of Set 1			
	R_{top2}	$R_{top2}-0.5$ mm	$R_{top2}+0.5$ mm
R_{top1}	**6.35**	6.30	6.38
$R_{top1}-0.5$ mm	6.30	6.28	6.32
$R_{top1}+0.5$ mm	6.37	6.33	6.38

Tolerance analysis of the height of Set 2			
	H_2	$H_2-0.5$ mm	$H_2+0.5$ mm
H_1	**7.12**	7.10	7.11
$H_1-0.5$ mm	7.09	7.06	7.09
$H_1+0.5$ mm	7.08	7.08	7.12

Tolerance analysis of the bottom radius of Set 2			
	R_{base2}	$R_{base2}-0.5$ mm	$R_{base2}+0.5$ mm
R_{base1}	**7.12**	7.08	7.09
$R_{base1}-0.5$ mm	7.09	7.05	7.10
$R_{base1}+0.5$ mm	7.16	7.09	7.11

Tolerance analysis of the top radius of Set 2			
	R_{top2}	$R_{top2}-0.5$ mm	$R_{top2}+0.5$ mm
R_{top1}	**7.12**	7.04	7.14
$R_{top1}-0.5$ mm	7.03	6.97	7.08
$R_{top1}+0.5$ mm	7.14	7.08	7.19

Tolerance analysis of the height of Set 3			
	H_2	$H_2-0.5$ mm	$H_2+0.5$ mm
H_1	**7.71**	7.72	7.72
$H_1-0.5$ mm	7.68	7.67	7.73
$H_1+0.5$ mm	7.72	7.71	7.73

Tolerance analysis of the bottom radius of Set 3			
	R_{base2}	$R_{base2}-0.5$ mm	$R_{base2}+0.5$ mm
R_{base1}	**7.71**	7.69	7.71
$R_{base1}-0.5$ mm	7.70	7.71	7.71
$R_{base1}+0.5$ mm	7.72	7.70	7.74

Tolerance analysis of the top radius of Set 3			
	R_{top2}	$R_{top2}-0.5$ mm	$R_{top2}+0.5$ mm
R_{top1}	**7.71**	7.64	7.76
$R_{top1}-0.5$ mm	7.65	7.58	7.69
$R_{top1}+0.5$ mm	7.76	7.71	7.82

Acknowledgements

The authors are grateful to Professor Du Guanxiang from Nanjing University of Posts and Telecommunications for his constructive suggestions on the simulation and experimental design. His guidance has been instrumental in shaping this research. This work was supported by the Natural Science Foundation of China (Grant No. 62375285) and the Research Project of the National University of Defense Technology (Grant No. 24-ZZCX-XXXX-01-04).

References

[1] Schmidt A B, Chekmenev E Y, Maissin H, Groß P R, Petersen S, Nagel L, Schilling F, Schwartz I, Reinheckel T, Hövener J and Knecht S 2024 *Anal. Sens.* **4** 1
[2] Li Y, Cheng H, Alhalili Z, Xu G and Gao G 2021 *J. Chin. Chem. Soc.* **68** 216
[3] Zhen Y Z, Yong B L, Liang C, Qiang Z and Yue S 2024 *Minerals* **14** 837
[4] Mendes B D L, Kontny A, Dudzisz K and Wilke F D H 2024 *Meteorit. Planet. Sci.* **59** 1577
[5] Hao Y P, Wen F F, Feng L, Li H D, Si X L, Jing W and Wei Q 2022 *IEEE Trans. Instrum. Meas.* **71** 0000101
[6] Han Y, Benjamin M and Ferruccio R 2023 *Opt. Express* **31** 27287
[7] Claire A M, Bryan A M, Stephan K, Kenichi O, David D A and Ania C B J 2016 *Nano Lett.* **16** 2450
[8] Song L Y, Ming Y T, Tian Q Y, Xu L, Xian B W and Jin Z 2020 *Nano-Micro Lett.* **12** 181
[9] Lettens J, Avramenko M, Vandevenne I, Chu A, Hengel P, Kern M, Anders J, Moens P, Goovaerts E and Cambré S 2024 *J. Magn. Reson.* **137** 1
[10] Niu L Y, Ren X H, Wang H L, Zhao X Y and You Z 2023 *Electron. Des. Eng.* **31** 99
[11] Liu Y, Kang A G, Li L H and Wu X 2019 *Safety in Coal Mines* **50** 122
[12] Srivatsa C, Chris M, April O, Emma H, Andrew I, Ian C, Scott D and Kai-Mei C F 2020 *Phys. Rev. Mater.* **4** 023402
[13] Gkika V, Kim Y, Matlashov A, Shin Y C, Semertzidis Y, Cantor R, Lohmeyer C, Aggarwal N and Geraci A 2024 *J. Low Temp. Phys.* **216** 386
[14] Yang S R, Wang Q W, Fu J Q and Kong J 2024 *Quantum Opt.* **30** 46
[15] Pan M C, Hu J F, Tian W G, Chen D X and Zhao J Q 2012 *Sensors Actuators A* **179** 92
[16] Almeida J M and Freitas P P 2009 *J. Appl. Phys.* **105** 07E722
[17] Wu D J, Li Z H, Tang J and Liu J 2023 *Micronanoelectron. Technol.* **60** 259
[18] Guo J M, Zhang Z H, Zhang T Y, Zhao X Y, Li C L, Yin L, Song F, Tao L Q, Yan J F, Liang L, Mi W and Han L 2024 *IEEE Sens. J.* **24** 19901
[19] Leroy P, Coillot C, Roux A F and Chanteur G M 2006 *IEEE Sens. J.* **6** 707
[20] Zhang X M, Bi Y, Chen G B, Liu J, Li J, Feng K Q, Lv C and Wang W J 2018 *AIP Adv.* **8** 125222
[21] Rafi A M, Nogina D, Penzar D, *et al*. 2025 *Nat. Biotechnol.* **43** 1373
[22] Oussous S A, Lail D M, Bouayadi R E and Amine A 2025 *IEEE Access* **13** 64810
[23] Padmavathi B, Dhivya S, Kavitha D, Banu A K and Karthikeyan S M 2024 *Int. J. Veh. Struct. Sys.* **16** 45
[24] Zhou Y X, Nie S H, Sun P F, Su L J and Gao Y 2024 *Micro Nanostructures* **195** 207985
[25] Xue Z, Sun C W, Zheng W H, Lv J C and Liu X G 2025 *Bioinformatics* **41** btae730
[26] Ye Q L, Wang W L and Wang Z 2024 *J. Zhejiang University (Eng. Sci.)* **58** 1107
[27] Ding L and Chong J F 2023 *J. Anyang Normal University* **2** 9
[28] Hwang S and Smith R 2012 *Korean J. Chem. Eng.* **29** 25
[29] Netrapalli P 2019 *J. Indian Inst. Sci.* **99** 201
[30] Zhu G L J, Li Y D and Zou C F 1996 *J. Magnetic Materials and Devices* **2** 50
[31] Ji Z Y, Ma Y, Wang Q and Dong C 2022 *J. Mat. Eng.* **50** 69
[32] Shu B 2024 *New Technology & New Process* **443** 107
[33] Leroy P, Coillot C, Roux A and Chanteur G 2009 *tm-Tech. Mess.* **73** 339
[34] Xie Y J 2020 *Magnetometry Based on the Ensemble Nitrogen-vacancy Centers in Diamond* (Ph.D. Dissertation) (Hefei: University of Science and Technology of China) (in Chinese)
[35] Aharoni A 1998 *J. Appl. Phys.* **83** 3432
[36] Li Z H, Wang T Y, Guo Q, Guo H, Wen H F, Tang J and Liu J 2021 *Acta Phys. Sin.* **70** 147601 (in Chinese)
[37] Wang P F, Yuan Z H, Huang P, Rong X, Wang M Q, Xu X K, Duan C K, Ju C Y, Shi F Z and Du J F 2015 *Nat. Commun.* **6** 6631
[38] Taylor J M, Cappellaro P, Childress L, Jiang L, Budker D, Hemmer P R, Yacoby A, Walsworth R and Lukin M D 2008 *Condens. Matter* **5** 810